coatings

MDPI

Article

Enhanced Methanol Electro-Oxidation in Hierarchical Au-Pt Dendrites Supported on Graphene-like Substrate

Zifeng Zhu [1,†], Yiming Zhao [1,†], Yongming Ruan [2], Xuexiang Weng [1,*] and Gesmi Milcovich [3,*]

[1] Key Laboratory of the Ministry of Education for Advanced Catalysis Materials, College of Chemistry and Materials Science, Zhejiang Normal University, Jinhua 321004, China; 15356970090@zjnu.edu.cn (Z.Z.); 2080513985@zjnu.edu.cn (Y.Z.)
[2] College of Life Sciences, Zhejiang Normal University, Jinhua 321004, China; ruanym@zjnu.cn
[3] Department of Life Sciences, University of Modena and Reggio Emilia, 41124 Modena, Italy
* Correspondence: xuexian@zjnu.cn (X.W.); gesmi.milcovich@unimore.it (G.M.)
† These authors contributed to this work equally.

Abstract: This study presents an easy and rapid two-step electrodeposition method for the synthesis of a novel hierarchical dendritic AuPt bimetallic nanocomposite electrode. Ascorbic acid served as both a reducing and directing agent, while a roughened carbon substrate facilitated the formation of the unique dendritic nanostructure. The structural and compositional properties of the synthesized material were comprehensively characterized using X-ray photoelectron spectroscopy (XPS), X-ray diffraction (XRD), selected area electron diffraction (SAED), and transmission electron microscopy (TEM). The resulting nanocomposite exhibited a significantly enhanced specific surface area of 6.97 m^2 g^{-1}, compared to commercial Pt/C. Electrochemical investigations demonstrated superior electrocatalytic activity and durability for methanol oxidation in the prepared AuPt nanocomposite electrode, suggesting its promising potential for fuel cell applications.

Keywords: methanol oxidation; dendritic nanogold; bimetallic nanocomposite; Pt nanoparticles

check for updates

Academic Editor: Arūnas Ramanavičius

Received: 20 February 2025
Revised: 6 April 2025
Accepted: 10 April 2025
Published: 12 April 2025

Citation: Zhu, Z.; Zhao, Y.; Ruan, Y.; Weng, X.; Milcovich, G. Enhanced Methanol Electro-Oxidation in Hierarchical Au-Pt Dendrites Supported on Graphene-like Substrate. *Coatings* **2025**, *15*, 458. https://doi.org/10.3390/coatings15040458

1. Introduction

Direct methanol fuel cells (DMFCs) have garnered significant attention as a promising clean energy source due to their high energy conversion efficiency, low operating temperature, and convenient fuel handling [1–4]. The electrochemical oxidation of methanol at the anode, commonly referred to as the methanol oxidation reaction (MOR), is a critical process that significantly influences the overall performance of DMFCs [5]. Platinum (Pt)-based catalysts, particularly Pt/C, are widely used for MOR due to their superior catalytic activity. However, their performance is often limited by susceptibility to poisoning from reaction intermediates such as CO, which leads to a decrease in long-term stability and efficiency [6,7].

To address these limitations, bimetallic and multimetallic catalysts have been explored as alternatives to enhance MOR kinetics and improve catalyst durability. Incorporating a second metal can modify the electronic and geometric properties of Pt, reduce CO poisoning effects, and enhance catalytic efficiency. Various metals, including Ru, Pd, Ag, Rh, and Au, have been investigated as potential co-catalysts [8–12]. Among these, Au is particularly attractive due to its unique ability to improve CO tolerance and modify the electronic structure of Pt, thereby improving catalytic stability and performance [12–15]. Studies have shown that Au promotes the formation of hydroxyl species at lower potentials, which aids in the oxidation and removal of CO intermediates. Additionally, the high stability and corrosion resistance of Au contribute to the long-term durability of Pt-based catalysts under electrochemical conditions.

Moreover, the design and synthesis of nanostructured catalysts with tailored morphologies have been extensively explored to further enhance catalytic performance [16–22]. The integration of these nanostructured catalysts with conductive support is crucial for optimizing their performance in DMFCs. Carbon-based materials, including graphene and its derivatives, have been widely employed as catalyst supports due to their high surface area and excellent electrical conductivity [23]. In particular, 3D graphene, owing to its high surface area, serves as an ideal catalyst substrate, facilitating increased catalyst loading and mitigating performance degradation caused by catalyst agglomeration and detachment. Chen et al. reported the direct growth of mesoporous $NiCo_2O_4$/3D graphene nanofiber composites exhibiting superior electrochemical activity and stability for methanol oxidation [24]. Similarly, Xie et al. synthesized a 3D graphene-based Pt catalyst (Pt/3D GNs (C)) demonstrating the excellent activity, stability, and CO poisoning resistance in the MOR [25]. The production of carbon-based support materials often entails complex and costly processes [26]. Recent advancements, such as the electrochemical exfoliation method introduced by Parvez et al., have demonstrated potential for producing graphene sheets through a more efficient and rapid approach [27]. This method involves the application of a direct current voltage to graphite in an electrolyte, leading to the expansion of graphite edges, the formation of cracks within the graphite layers, and ultimately, the exfoliation of graphene flakes.

In our previous research, we created a 3D graphene-like surface via electrochemical pretreatment of the pencil lead electrode (EPLE). The EPLE enhanced the electrode surface area and facilitated the electron transfer ability within 5 min without any hazardous chemicals added [28,29]. In this work, we present a low-cost strategy for fabricating hierarchical dendritic Au-Pt microstructures directly on the EPLE. The resulting Au-Pt/EPLE composite was subjected to comprehensive characterization to elucidate its structural and compositional properties. The electrocatalytic activity of the prepared catalyst towards the methanol oxidation reaction (MOR) was evaluated and compared to commercial Pt/C to assess its performance enhancement.

2. Experimental

2.1. Reagents

The pencil lead electrode (2B, 0.5 mm in diameter) was purchased from Youli Stationery Co. Ltd. (Ningbo, China). Chloroauric acid ($HAuCl_4 \cdot 4H_2O$) and chloroplatinic acid ($H_2PtCl_6 \cdot 6H_2O$) were purchased from Sigma-Aldrich (St. Louis, MO, USA). Sodium sulfate (Na_2SO_4) and ascorbic acid (AA) were bought from Aladdin Chemical Reagent Company (Shanghai, China). All reagents were of analytical grade and used as received. Redistilled water was used in all experiments.

2.2. Characterization

The morphology, microstructure, and elemental composition of the synthesized materials were investigated using a combination of characterization techniques. Scanning electron microscopy (SEM) images were acquired on a Hitachi S-4800 scanning electron microscope (Hitachi, Tokyo, Japan). Transmission electron microscopy (TEM) and high-resolution transmission electron microscopy (HRTEM) analyses were performed on a JEM-2100F transmission electron microscope (JEOL, Tokyo, Japan) equipped with selective area electron diffraction (SAED) capabilities. These techniques provide detailed information on the size, shape, and crystallographic orientation of the deposited nanoparticles. X-ray photoelectron spectroscopy (XPS) was employed to elucidate the elemental composition and surface chemistry of the samples. The analyses were conducted using a K-Alpha XPS spectrometer (Thermo Fisher Scientific, Waltham, MA, USA) equipped with Al Kα X-ray radiation (1486.6 eV) as the excitation source. X-ray diffraction (XRD) patterns were obtained using a Rigaku Dmax-2000 diffractometer (Bruker Co., Bremen, Germany) with Cu Kα radiation to identify the crystal phases present in the materials. Finally, the quantitative determination of deposited Pt was achieved through inductively coupled plasma atomic emission spectrometry (ICP-AES) using a spectrometer from Thermo Fisher Scientific Co., Ltd. (Waltham, MA, USA).

2.3. Deposition of Hierarchical Dendritic PtNPs/AuDNs Microstructures on EPLE

For the deposition of AuDNs, the EPLEs were immersed in $HAuCl_4$ solutions using the *i-t* (current–time) method. The concentrations of $HAuCl_4$ (1.27, 1.85, 3.44, and 6.03 mM), electrodeposition potentials (−0.5 V, −0.3 V, −0.1 V, 0.1 V, and 0.3 V), and deposition durations (600, 1200, 3600, 5400, and 7200 s) were optimized. Following deposition, the obtained AuDNs/EPLE was thoroughly rinsed with deionized water and dried at RT.

Subsequently, platinum nanoparticles (PtNPs) were deposited onto the AuDNs/EPLE composite electrode using the i-t (current–time) method at a potential of −0.2 V. The composite electrode was immersed in 10 mL of 0.1 M phosphate-buffered saline (PBS, pH 7.4), containing 0.01 M ascorbic acid (AA) and 3.44 mM H_2PtCl_6, corresponding to the optimized concentration of $HAuCl_4$. The deposition time was varied at intervals of 5, 10, 20, 30, and 60 mins. Following the optimization of the deposition time, different concentrations of H_2PtCl_6 were tested, with Pt:Au molar ratios of 1:2, 1:1, 2:1, and 3:1, to further optimize the deposition of platinum nanoparticles (PtNPs) onto the AuNPs/EPLE composite. Finally, the obtained PtNPs/AuDNs/EPLE were subjected to multiple rinsing cycles with deionized water and subsequent air drying.

2.4. Electrochemical Measurements

All electrochemical measurements were conducted using a CHI 660C electrochemical workstation (Shanghai Chenhua Instrumental Co., Ltd., Shanghai, China) at an ambient temperature. A standard three-electrode configuration was employed, with a PtNPs/AuDNs/EPLE serving as the working electrode, a platinum wire as the counter electrode, and a saturated calomel electrode (SCE) as the reference electrode.

The electrochemically active surface area (ECSA) of the AuDNs/EPLE can be determined by calculating the charge in 0.5 M H_2SO_4 in a potential window of 0.6 to 1.5 V through cyclic voltammetry consumed during the reduction of gold oxide in the negative scan. This is based on the assumption that a monolayer of Au oxide is reduced and that the charge density required to reduce this monolayer per unit area is 386 $\mu C \cdot cm^{-2}$. The ECSA is then calculated using the following equation [30]:

$$\text{ECSA}\ (\text{cm}^2) = \frac{Q_0}{Q_{0s}} \tag{1}$$

where Q_0 represents the charge of the oxide-reduction peak from the backward scan (μC); Q_{0s} (386 $\mu C\ cm^{-2}$) is the charge density required to reduce monolayer oxygen.

For the Pt/C and $PtNPs_{(20min)/}$AuGNs/EPLE electrodes, the ECSA was assessed by quantifying the hydrogen adsorption/desorption charges within a potential window of −0.2 to 1.4 V in 0.5 M H_2SO_4 through cyclic voltammetry (CV) [31]. It is calculated using the following equation:

$$\text{ECSA}\ (\text{cm}^2\ \text{g}{-}^{1}{}_{\text{Pt}}) = \frac{Q_H}{210 m_{Pt}} \tag{2}$$

where Q_H is the charge obtained from hydrogen desorption (μC), m_{Pt} is the Pt loading amount of the electrode (mg), and 210 is the charge associated with monolayer adsorption of hydrogen on the surface of Pt (μC cm^{-2}). The electrocatalytic activity of the catalyst-modified electrodes toward the methanol oxidation reaction (MOR) was evaluated using CV in 1.0 M NaOH with varying concentrations of methanol. The stability of the electrodes was examined via chronoamperometry at a constant potential of −0.3 V for 10,000 s in a 1.0 M NaOH solution containing 0.5 M methanol.

3. Results and Discussions

3.1. Preparation and Characterization of AuDNs/EPLE

To prepare AuDNs/EPLEs, the deposition potential, electrolyte concentration, and deposition time were first optimized. Figure S1A depicts the cyclic voltammograms (CVs) of AuDNs/EPLE at different potentials in 0.5 M H_2SO_4 solution. The corresponding electrochemical active surface area (ECSA) was calculated for each deposition potential (Figure S1A inset). The results revealed that the electrode deposited at −0.3 V exhibited the highest ECSA. Additionally, this deposition potential led to the highest current density with 5 mM $[Fe(CN)_6]^{3-}$ (Figure S1B).

The concentration of $HAuCl_4$ remarkably influenced the electrochemical performance of AuDNs/EPLE too. As shown in Figure S1C,D, increasing the $HAuCl_4$ concentration from 1.27 mM to 3.44 mM resulted in a progressive increase in the ECSA and the corresponding current density with 5 mM $[Fe(CN)_6]^{3-}$. However, a further increase in concentration led to a decrease in both ECSA and current density.

Under the optimized conditions of −0.3 V deposition potential and 3.44 mM $HAuCl_4$ concentration, the influence of deposition time on the electrochemical properties of AuDNs/EPLE was investigated. Figure S1E demonstrates that the ECSA increased with increasing deposition time. Indeed, Figure S1F shows that the highest current density was achieved at a deposition time of 3600 s. Considering reagent and time efficiency, 3600 s was chosen as the optimal deposition time for subsequent experiments.

These optimizations allowed us to reach a balance between maximizing the surface area of AuDNs for enhanced electron transfer and maintaining a well-defined morphology for optimal catalytic activity.

SEM images in Figure 1A,B reveal a well-defined dendritic structure, with gold uniformly distributed across the EPLE surface. EDS mapping (Figure 1C) demonstrates uniform distributions of carbon (C), oxygen (O), and gold (Au), with a particularly strong signal for Au and relatively weaker signals for C, indicative of the consistent gold coverage on the EPLE surface. Furthermore, Figure 1D presents the quantitative elemental composition obtained from the EDS analysis, with atomic percentages of 54.72% C, 2.50% O, and 42.78% Au.

The XRD pattern in Figure S2A confirms the presence of metallic gold, with characteristic peaks related to the (111), (200), (220), and (311) crystal planes, while the diffraction peak at 2θ = 26.5° and 54.7° corresponded to the (002) and (004) graphite hexagonal structure. The high-resolution XPS spectrum in Figure S2B further confirms the presence of metallic gold, with binding energies at 83.91 eV and 87.63 eV for Au $4f_{7/2}$ and Au $4f_{5/2}$, respectively [32]. The electrochemical performance of AuDNs/EPLE was evaluated by cyclic voltammetry in a solution containing 5 mM $[Fe(CN)_6]^{3-}/[Fe(CN)_6]^{4-}$. As shown in Figure S2C, the AuDNs/EPLE exhibited a higher current (approximately 1.7 times greater) and a narrower ΔE_p compared to the bare EPLE. This enhanced electrochemical performance can be associated with the increased surface area and improved electron transfer kinetics provided by the dendritic gold nanoparticles.

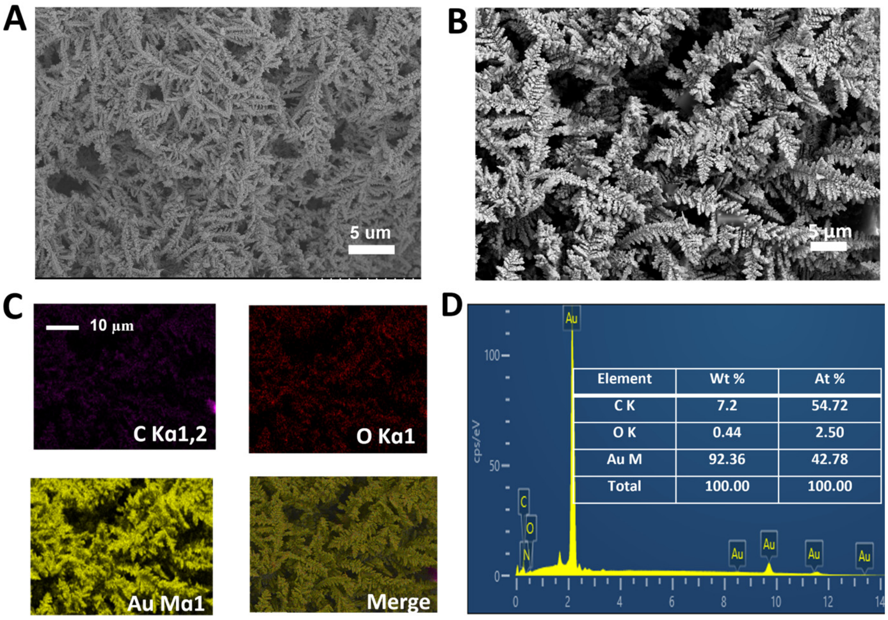

Element	Wt %	At %
C K	7.2	54.72
O K	0.44	2.50
Au M	92.36	42.78
Total	100.00	100.00

Figure 1. (**A**,**B**) SEM images, (**C**) EDS elemental mapping, and (**D**) EDS spectrum of AuDNs/EPLE.

3.2. Optimization of Electrodeposition Conditions of Pt Particles on AuDNs/EPLE

The formation of Pt nanoparticles on AuDNs/EPLE as a function of deposition time was probed via cyclic voltammetry in N_2-saturated 0.5 M H_2SO_4 (Figure 2A). Hydrogen adsorption/desorption peaks, observed between −0.1 and 0.2 V, were employed to estimate the ECSA. Reduction peaks attributed to Pt oxide and Au oxide appeared at approximately +0.4 V and +0.9 V, respectively [33]. As deposition time increased, the Au oxide reduction peak diminished, while the Pt oxide reduction peak intensified [34], indicating progressive Pt coverage of the Au nanostructure.

Figure 2B illustrates the methanol oxidation reaction (MOR) on electrodes with varying Pt deposition times. Distinct redox peaks were observed during both forward and reverse scans. The sharp forward peak at −0.2 V is attributed to methanol oxidation and CO intermediate formation [35], while the reverse peak at −0.4 V corresponds to the removal of residual carbonaceous species [36]. The concentration of NaOH (1 M) plays a crucial role in the MOR by influencing reaction kinetics, intermediate formation, and catalyst stability [36]. While lower concentrations of OH^- may result in slower reaction rates and incomplete removal of intermediates like CO_{ads}, excessive OH^- can promote undesirable side reactions such as the oxygen evolution reaction (OER), which competes with methanol oxidation and reduces overall efficiency. Furthermore, the formation of Au-OH at lower potentials in alkaline media facilitates CO removal, enhancing Pt's anti-poisoning ability [37]. Peak current density increased with deposition time up to 20 min, correlating with an increase in active Pt sites [38,39]. Further deposition led to a decline in peak current density, possibly due to excessive Pt coverage inhibiting CO oxidation and poisoning the catalyst surface [40].

The electrochemical behavior of electrodes with varying Pt/Au molar ratios was investigated in N_2–saturated 0.5 M H_2SO_4 (Figure 2C). When the electrode consisted of Au dendrites on the EPLE (pure Au, AuDNs/EPLE), only one reduction peak at approximately 0.89 V was observed. Similarly, for Pt nanoparticles on the EPLE (pure Pt, PtNPs/EPLE), the single reduction peak appeared at around 0.39 V. As the Pt/Au ratio increased, a progressive decrease in the Au oxide reduction peak at +0.89 V was observed (Figure 2E), indicating enhanced Pt coverage on the Au nanostructure. However, even at Pt/Au ratios of 2:1 and 3:1, the persistence of this peak suggests incomplete Au encapsulation. These findings imply the formation of Pt nanostructures on the Au surface rather than the formation of an alloy.

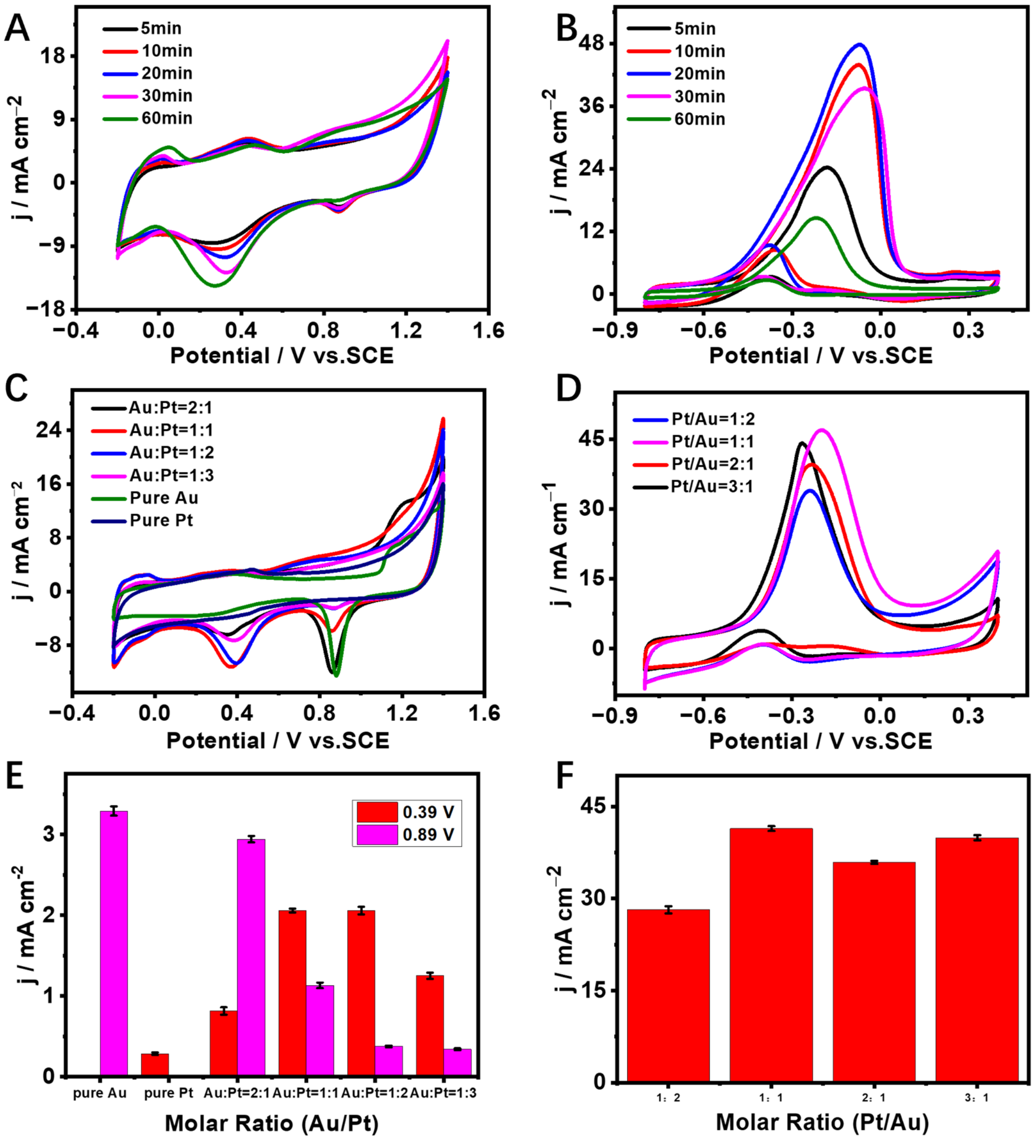

Figure 2. CVs of PtNPs/AuDNs/EPLE (**A**) in 0.5 M H_2SO_4 and (**B**) methanol oxidation in 0.1 M NaOH with 0.25 M CH_3OH recorded at different Pt deposition times. CVs comparing various Pt/Au molar ratios (**C**) in 0.5 M H_2SO_4 and (**D**) in 0.1 M NaOH with 0.25 M CH_3OH. (**E**) Bar charts of current densities from Figure 2C at +0.89 V and +0.39 V. (**F**) Bar charts of current densities from Figure 2D showing methanol oxidation performance.

Figure 2D presents the methanol oxidation behavior of electrodes with different Pt/Au ratios. The 1:1 ratio exhibited the highest peak current density (Figure 2F), indicating optimal catalytic activity. A lower Pt/Au ratio results in a limited number of active Pt sites, thereby restricting the catalytic performance of the electrode. Conversely, at higher Pt/Au ratios, excessive Pt deposition leads to the formation of thicker Pt layers, which hinder access to highly active Pt-Au interface sites. Moreover, an increase in Pt coverage promotes the formation of Pt-OH species, which can poison active sites and reduce catalytic efficiency [41]. The superior catalytic performance at a Pt/Au ratio of 1:1 is attributed to the synergistic interplay between Au and Pt, which optimizes both electronic and geometric effects, facilitating enhanced methanol oxidation activity.

3.3. Characterization of PtNPs$_{(20min)}$/AuDNs/EPLE

The morphology of the optimized PtNPs$_{(20min)}$/AuDNs/EPLE was examined using SEM. As shown in Figure 3A, the EPLE surface was densely covered with dendritic microstructures ranging from 10 to 20 μm in length. High-magnification SEM in Figure 3B revealed a hierarchical structure characterized by a central backbone with secondary and tertiary branches. The EDS mapping shown in Figure 3C confirmed the uniform distribution of carbon (C), oxygen (O), platinum (Pt), and gold (Au) on the surface. Notably, the merged image highlighted a pronounced concentration of Pt along the dendritic sides and edge planes. Furthermore, Figure 3D presented the quantitative elemental composition derived from EDS analysis, revealing atomic percentages of 66.92% C, 4.82% O, 11.90% Pt, and 16.36% Au.

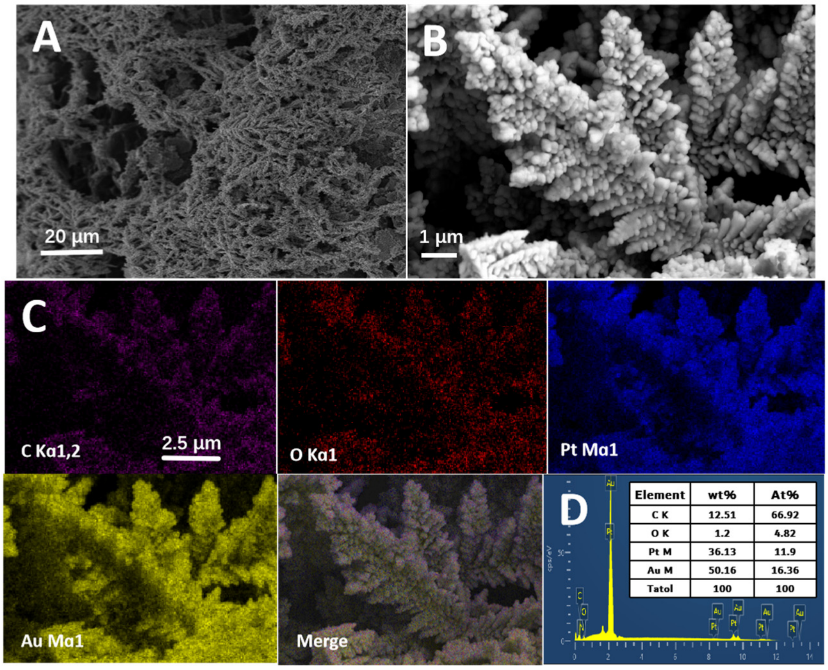

Element	wt%	At%
C K	12.51	66.92
O K	1.2	4.82
Pt M	36.13	11.9
Au M	50.16	16.36
Tatol	100	100

Figure 3. (**A**,**B**) SEM images of PtNPs$_{(20\mathrm{min})}$/AuDNs/EPLE. (**C**) EDS elemental mapping and (**D**) EDS spectrum of PtNPs$_{(20\mathrm{min})}$/AuDNs/EPLE.

TEM analysis (Figure 4A,B) provided additional insights into the morphology and crystal structure of the nanoparticles. The selected-area electron diffraction (SAED) pattern (inset of Figure 4B) indicated the polycrystalline nature of the deposited nanoparticles. Lattice fringes observed on the dendritic stem (Figure 4C) and second-order branches (Figure 4D) corresponded to the (111) planes of Au and the (111) and (200) planes of Pt, respectively [42]. XRD analysis confirmed the crystalline structure of PtNPs$_{(20\mathrm{min})}$/AuDNs/EPLE (Figure 4E). Sharp diffraction peaks at 39.9°, 46.6°, 67.8°, and 82.1° corresponded to the (111), (200), (220), and (311) planes of Au or Pt, respectively. The overlap of Pt and Au peaks was attributed to their similar crystal structures [15]. Peaks at 26.1° and 53.0° corresponded to the (002) and (004) graphite hexagonal structure.

XPS analysis was conducted to elucidate the elemental composition and oxidation states of PtNPs$_{(20\mathrm{min})}$/AuDNs/EPLE. The survey spectrum (Figure 5A) confirmed the presence of Au, Pt, O, and C. High-resolution Au 4f spectra (Figure 5B) exhibited peaks at 83.5 and 87.2 eV, attributed to Au 4f$_{7/2}$ and Au 4f$_{5/2}$ of Au^0, respectively [43]. The Pt 4f spectrum (Figure 5C) was deconvoluted into four peaks. The dominant peaks at 70.2 and 73.5 eV corresponded to Pt 4f$_{5/2}$ and Pt 4f$_{7/2}$ of Pt^0. Peaks at 71.0 and 75.0 eV indicated the presence of Pt^{2+} which might come from the PtO during exposure to air [44]. The relative peak intensities indicate that Pt^0 is the predominant species, with the Pt^0 fraction in Pt^0/(Pt^0 + Pt^{2+}) estimated to be 0.72.

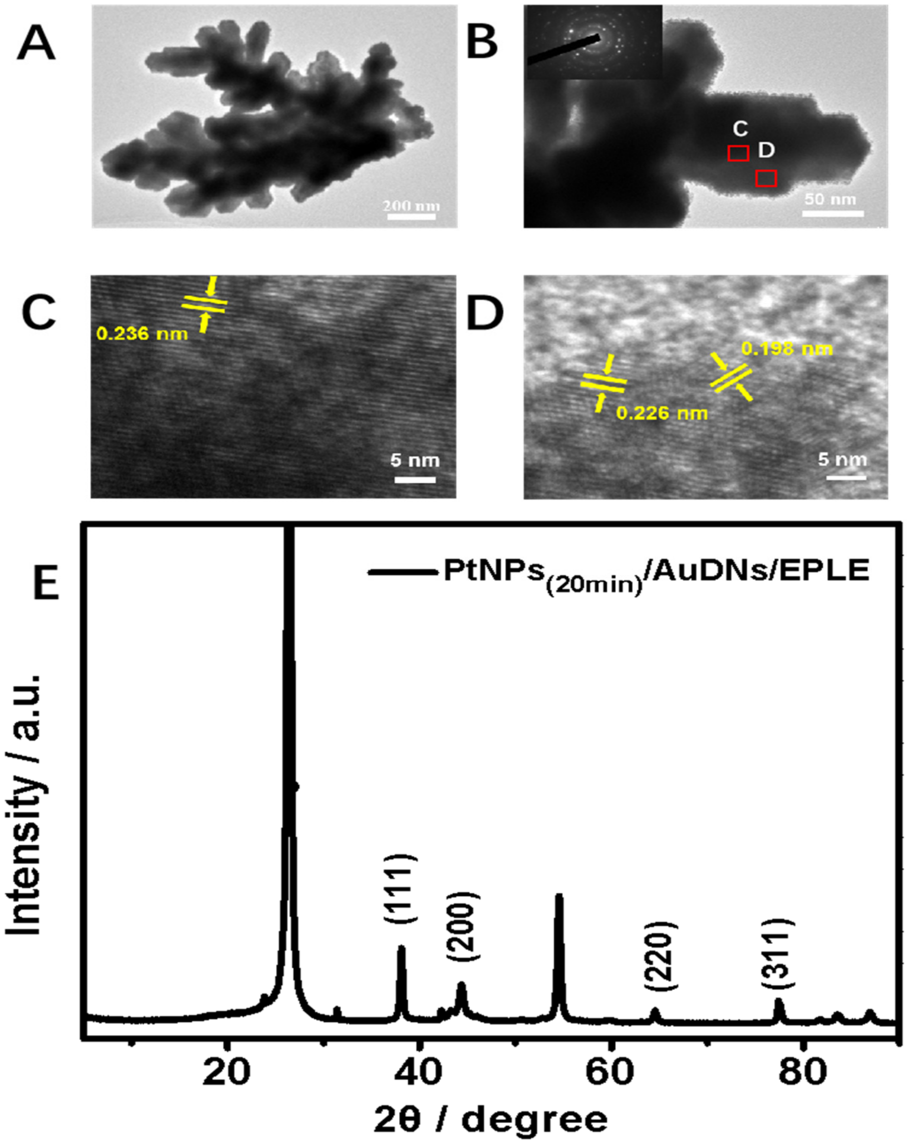

Figure 4. (**A**,**B**) TEM and (**C**,**D**) HRTEM images of PtNPs$_{(20min)}$/AuDNs/EPLE. The inset in Figure 4B shows the SAED pattern of PtNPs$_{(20min)}$/AuDNs/EPLE. (**E**) The XRD pattern of PtNPs$_{(20min)}$/AuDNs/EPLE.

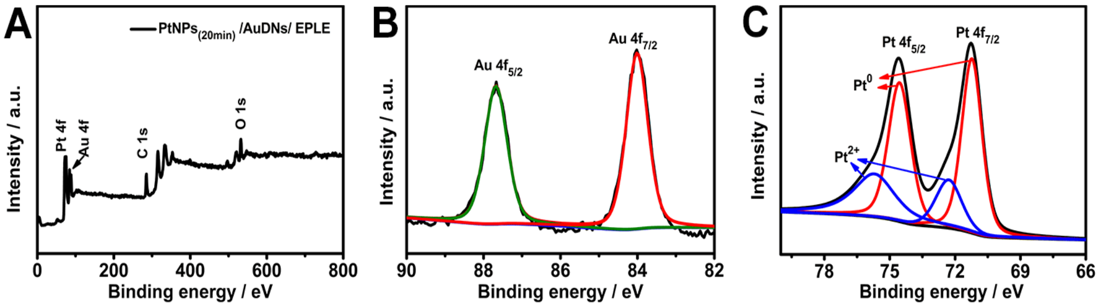

Figure 5. XPS spectra of the PtNPs$_{(20min)}$/AuDNs/EPLE: (**A**) survey spectrum, (**B**) high-resolution Au 4f spectra, and (**C**) high-resolution Pt 4f spectra.

3.4. Formation Mechanism of PtNPs$_{(20min)}$/AuDNs/EPLE

To elucidate the formation mechanism of hierarchical dendritic PtNPs$_{(20min)}$/AuDNs/EPLE, the substrate surface roughness was investigated. SEM images (Figure 6A, A1, A2) revealed that dendritic nanostructures on PtNPs$_{(20min)}$//AuDNs/EPLE were wider and larger compared to those on PtNPs$_{(20\text{min})}$//AuDNs/PLE (Figure 6B), indicating enhanced three-dimensional growth. These differences highlight the critical role of electrochemical expansion in modifying the PLE surface. This pretreatment introduced oxygen-containing functional groups (e.g., –OH, C=O, C–O–C), which increased surface hydrophilicity and roughness [28]. The resulting high surface area and improved wettability improve the overall electrolyte contact and facilitate effective ion transport to the electrode surface. While improved ion access is crucial for initiating nucleation, the dendritic growth process is still governed by localized mass transport and reaction kinetics. Under the applied potential of −0.3 V, the reduction of $AuCl_4^-$ occurs at a moderate rate, which allows for diffusion-limited aggregation (DLA) to dominate, favoring anisotropic and branched crystal growth [45–47]. This controlled kinetic regime, coupled with the EPLE's favorable surface properties, drives the formation of well-defined dendritic gold structures. In contrast, if the local diffusion of $AuCl_4^-$ is too fast or nucleation occurs too rapidly, the system may shift away from DLA conditions, leading to the formation of more compact, less ordered gold structures [48].

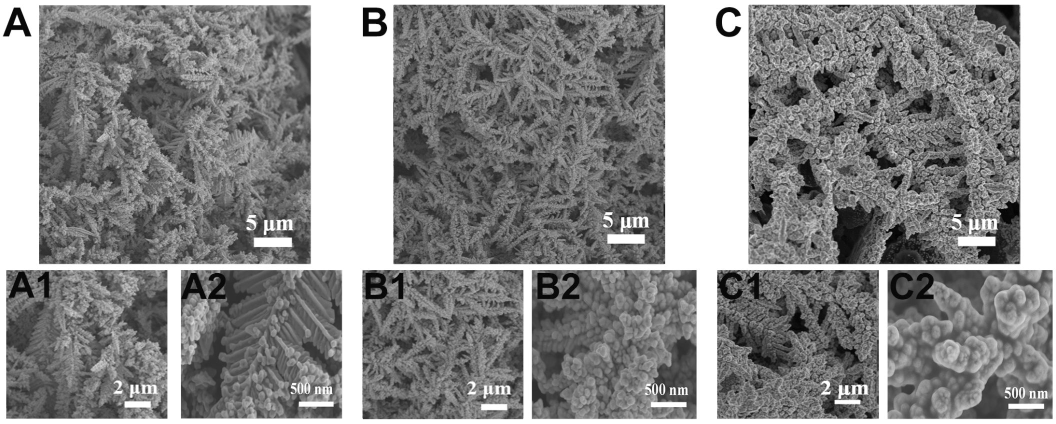

Figure 6. Typical SEM images of (**A**) PtNPs$_{(20\text{min})}$/AuDNs/EPLE, with (**A1**,**A2**) showing magnified views of selected regions in (**A**); (**B**) PtNPs$_{(20\text{min})}$/AuDNs/PLE with AA reduction, with (**B1**,**B2**) showing magnified views of (**B**); and (**C**) PtNPs$_{(20\text{min})}$/AuDNs/EPLE without AA reduction, with (**C1**,**C2**) showing magnified views of (**C**).

The influence of ascorbic acid (AA) on Pt structure formation was investigated. In the absence of AA, Pt and Au particles formed an irregular overlayer, lacking the distinct dendritic morphology observed in the presence of AA (Figure 6C). The presence of AA promoted the formation of well-defined dendritic Pt architectures, attributable to the synergistic effect of AA-mediated chemical reduction and electrochemical deposition. This synergy accelerated Pt nucleation, particularly along the high-energy edges and side planes of the Au dendrites, as confirmed by SEM elemental mapping of the PtNPs$_{(20\text{min})}$/AuDNs/EPLE composite (Figure 3C).

AA further modulates the electrochemical environment by adsorbing onto Au surfaces, altering surface energy and wettability [49–52]. This promotes selective Pt deposition at high-energy sites while passivating smoother regions. Additionally, the hydroxyl (-OH) and carboxyl (-COOH) groups of AA interact with Pt ions, influencing their diffusion and directing growth along dendritic sidewalls, thereby minimizing central aggregation. Figure 7 illustrates the proposed growth mechanism, emphasizing AA's role in spatially controlled Pt deposition and the formation of hierarchical dendritic structures.

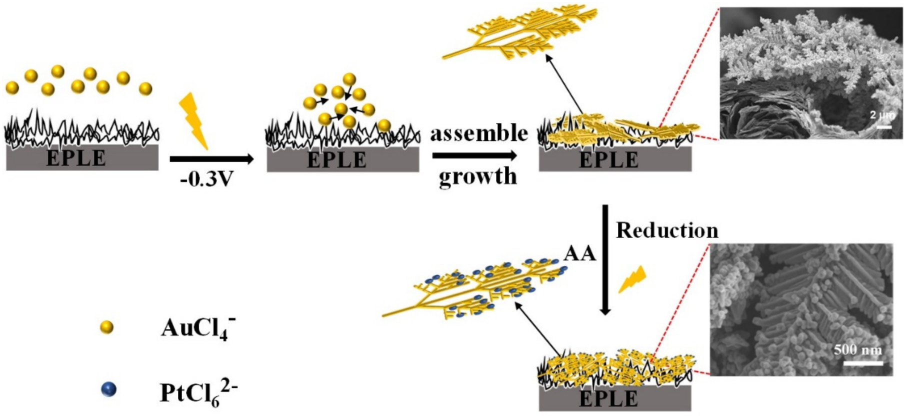

Figure 7. The formation mechanism of $PtNPs_{(20min)}$/AuDNs/EPLE.

3.5. The Catalytic Activity Toward the Oxidation of Methanol

To evaluate the synergistic effect of bimetallic nanostructures on the pre-expanded PLE, the active areas of PLE, EPLE, AuDNs/EPLE, $PtNPs_{(20min)}$/EPLE, $PtNPs_{(20min)}$/AuDNs/PLE, and $PtNPs_{(20min)}$/AuDNs/EPLE were determined (Figure 8A). EPLE exhibited a threefold increase compared to PLE, providing more active sites for subsequent metal deposition. $PtNPs_{(20min)}$/AuDNs/EPLE demonstrated the highest active areas, indicating a synergistic enhancement from the combined Au and Pt nanoparticles.

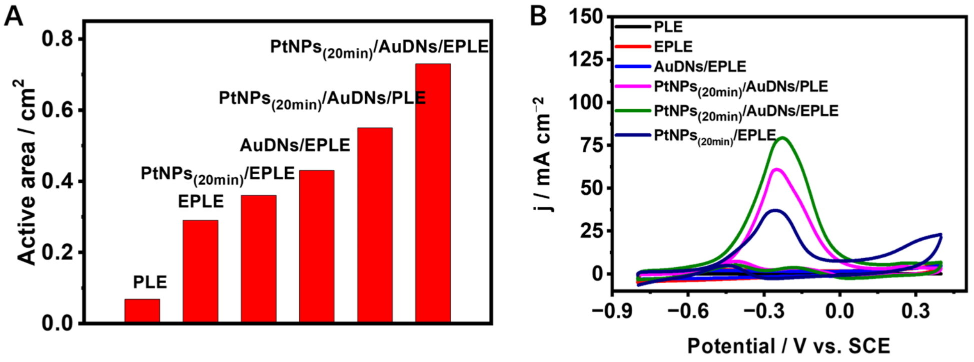

Figure 8. (**A**) The active areas of different electrodes. (**B**) CV curves of different electrodes in 1 M NaOH containing 0.5 M CH_3OH with a scan rate of 50 mV s^{-1}.

The electrocatalytic performance of these electrodes towards methanol oxidation was assessed in N_2-saturated 1 M NaOH containing 0.5 M methanol via CV (Figure 8B). PLE, EPLE, and AuDNs/EPLE exhibited negligible methanol oxidation activity. $PtNPs_{(20min)}$/Au DNs/EPLE displayed the highest current density, approximately 1.27 times that of $PtNPs_{(20min)}$/AuDNs/PLE. This enhancement is attributed to the increased surface area of the 3D graphene-like structure, providing more active Au and Pt sites for methanol adsorption and oxidation. Furthermore, the current density of $PtNPs_{(20min)}$/AuDNs/EPLE was nearly twice that of $PtNPs_{(20min)}$/EPLE, whereas AuDNs/EPLE exhibited a negligible current, further highlighting the synergistic interaction between platinum and gold. Notably, the forward-to-backward current density ratio (I_f/I_b) for $PtNPs_{(20min)}$/AuDNs/EPLE was approximately 25, significantly higher than the value of 8 observed for $PtNPs_{(20min)}$/EPLE. This elevated I_f/I_b ratio indicates enhanced tolerance to CO poisoning, a critical factor in electrocatalysis, as a higher ratio suggests more effective oxidation of CO intermediates.

The superior catalytic performance of the $PtNPs_{(20min)}$/AuDNs/EPLE system can be attributed to the cooperative effect between Pt and Au. While platinum serves as the primary catalytic site, the dendritic gold structure enhances the overall reaction kinetics by facilitating electron transfer and promoting the oxidation of adsorbed CO into CO_2.

The electrocatalytic activity of PtNPs$_{(20min)}$/AuDNs/EPLE was evaluated via cyclic voltammetry (CV) in 0.5 M H_2SO_4 (Figure 9A). The calculated ECSA of PtNPs$_{(20min)}$/AuDNs /EPLE was 6.97 $m^2\ g^{-1}$ (Pt loading: 0.1258 mg), significantly exceeding that of commercial Pt/C (10 wt.%) at 2.88 $m^2\ g^{-1}$ (Figure 9B). This enhancement is attributed to the unique dendritic Au-Pt structure and 3D graphene-like structure, which provide a larger surface area and prevent nanoparticle agglomeration.

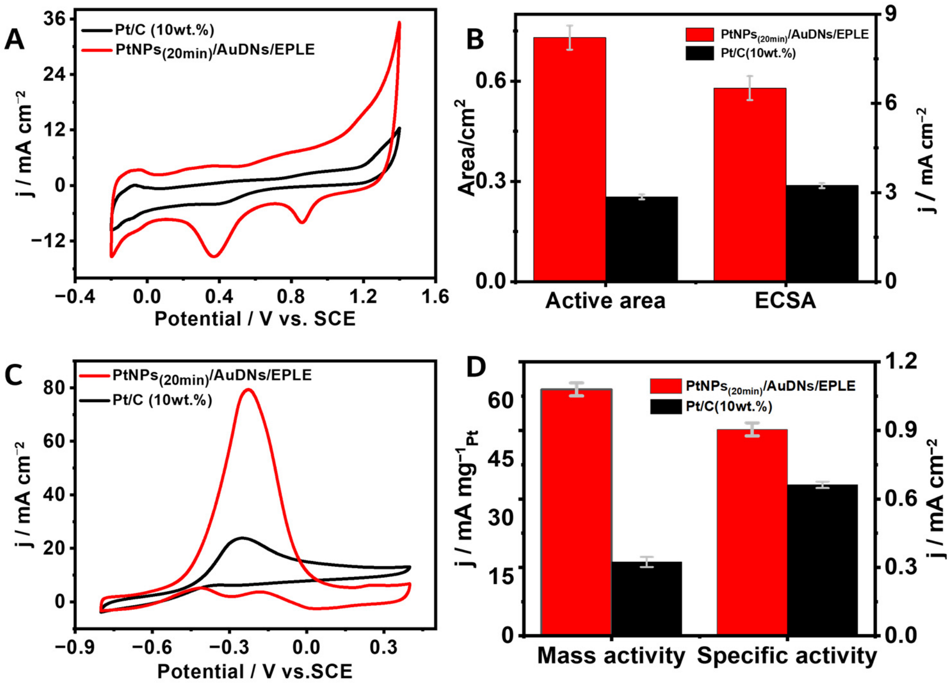

Figure 9. (**A**) CVs of PtNPs$_{(20min)}$/AuDNs/EPLE and commercial Pt/C (10 wt.%) at a rate scan of 50 mV/s in a 0.5 M H_2SO_4 solution. (**B**) The active area and ECSA for each catalyst. (**C**) CVs of PtNPs$_{(20min)}$/AuDNs/EPLE and Pt/C (10 wt.%) in 1.0 M NaOH containing 0.5 M CH_3OH. (**D**) The corresponding specific and mass activity.

The electrocatalytic performance towards methanol oxidation was assessed by CV (Figure 9C). PtNPs$_{(20min)}$/AuDNs/EPLE exhibited a forward peak current density (j_f) of 80 mA cm^{-2}, four times higher than commercial Pt/C (10 wt.%). Moreover, the onset potential of PtNPs$_{(20min)}$/AuDNs/EPLE was more negative, indicating superior catalytic activity. The higher j_f/j_b ratio (14.95) of PtNPs$_{(20min)}$/AuDNs/EPLE compared to commercial Pt/C (10 wt.%) (3.82) suggests improved resistance to CO poisoning [53]. The calculated specific activity (the catalytic activity per unit ECSA of platinum) and mass activity (the catalytic performance per unit mass of platinum) of PtNPs$_{(20min)}$/AuDNs/EPLE (0.905 mA cm^{-2} and 63.10 mA mg^{-1}Pt, respectively) surpassed those of commercial Pt/C (10 wt.%), confirming enhanced catalytic performance (Figure 9D).

The electrocatalytic stability and durability of PtNPs$_{(20min)}$/AuDNs/EPLE were evaluated through chronoamperometry and cyclic voltammetry in 1 M NaOH containing 0.5 M CH_3OH. As shown in Figure 10A, the catalyst exhibited excellent stability during 10,000 s of continuous chronoamperometric testing at −0.2 V, maintaining a current density of 5.85 mA cm^{-2}, significantly surpassing the performance of Pt/C (10 wt.%) at 4.40 mA cm^{-2}. This enhanced stability is attributed to the catalyst's resistance to CO poisoning. Additionally, the catalyst demonstrated superior long-term stability during cyclic voltammetry, retaining 99.5% and 83.6% of its initial current density after 20 and 100 cycles, respectively (Figure 10B). These findings collectively underscore the remarkable stability and durability of the PtNPs$_{(20min)}$/AuDNs/EPLE catalyst for methanol oxidation.

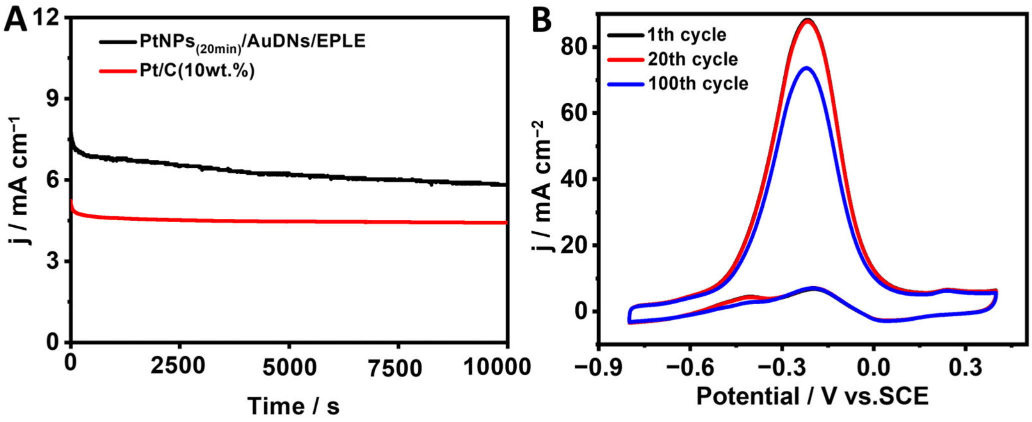

Figure 10. (**A**) Chronoamperometric curves of PtNPs$_{(20min)}$/AuGNs/EPLE and Pt/C(10wt.%) in 1.0 M NaOH solution containing 0.5 M methanol at a potential of −0.2 V; (**B**) cyclic voltammetry (CV) curves of PtNPs$_{(20min)}$/AuGNs/EPLE in N_2-saturated 1.0 M NaOH solution containing 0.5 M methanol after different cycles. Scan rate: 50 mV s^{-1}.

4. Conclusions

In summary, this study successfully fabricated hierarchical dendritic PtNPs$_{(20min)}$/Au DNs/EPLE microstructures through an easy and scalable two-step electrodeposition process, offering a promising alternative to traditional hydrothermal methods. Comprehensive characterization confirmed the formation of the desired hierarchical architecture, which contributed to a significantly enhanced specific surface area. The resulting electrode exhibited superior electrocatalytic performance for methanol oxidation compared to commercial Pt/C, demonstrating improved activity, durability, and tolerance to CO poisoning. The observed synergistic effects between Au and Pt within the dendritic nanostructure are attributed to the enhanced catalytic properties. This work provides a valuable strategy for the design and synthesis of high-performance electrocatalysts for fuel cell applications.

Supplementary Materials: The following supporting information can be downloaded at https://www.mdpi.com/article/10.3390/coatings15040458/s1. Figure S1: Electrochemical characterization of AuDNs/EPLE electrodes prepared under different conditions. Figure S2: Characterization of AuDNs/EPLE electrodes.

Author Contributions: Conceptualization and supervision, G.M. and Y.R.; methodology, Z.Z.; software, Y.Z.; Investigation, Y.Z.; resources, X.W.; data curation, Z.Z. and Y.Z.; writing—original draft preparation, Z.Z.; writing—review and editing, X.W. and G.M.; project administration, Y.R.; funding acquisition, G.M. and X.W. All authors have read and agreed to the published version of the manuscript.

Funding: This work was financially supported by Natural Science Foundation of Zhejiang Province, China (LY18B050004). European Union–NextGenerationEU through the Italian Ministry of University and Research under NRRP, M4 C2-I1.3 Project PE_00000019 "HEAL ITALIA" to GM, CUP 425 E93C22001860006 of University of Modena and Reggio Emilia is gratefully acknowledged. The views and opinions expressed are those of the authors only and do not necessarily reflect those of the European Union or the European Commission. Neither the European Union nor the European Commission can be held responsible for them.

Data Availability Statement: The data presented in this study are available on request from the first author.

Conflicts of Interest: The authors declare no conflicts of interest.

References

1. Huang, L.; Niu, H.; Xia, C.; Li, F.-M.; Shahid, Z.; Xia, B.Y. Integration Construction of Hybrid Electrocatalysts for Oxygen Reduction. *Adv. Mater.* **2024**, *36*, 2404773. [CrossRef]
2. Din, M.A.U.; Idrees, M.; Jamil, S.; Irfan, S.; Nazir, G.; Mudassir, M.A.; Saleem, M.S.; Batool, S.; Cheng, N.P.; Saidur, R. Advances and challenges of methanol-tolerant oxygen reduction reaction electrocatalysts for the direct methanol fuel cell. *J. Energy Chem.* **2023**, *77*, 499–513. [CrossRef]
3. Wang, J.; Zhang, B.; Guo, W.; Wang, L.; Chen, J.; Pan, H.; Sun, W. Toward Electrocatalytic Methanol Oxidation Reaction: Longstanding Debates and Emerging Catalysts. *Adv. Mater.* **2023**, *35*, 2211099. [CrossRef]
4. Burhan, H.; Arikan, K.; Alma, M.H.; Nas, M.S.; Karimi-Maleh, H.; Sen, F.; Karimi, F.; Vasseghian, Y. Highly efficient carbon hybrid supported catalysts using nano-architecture as anode catalysts for direct methanol fuel cells. *Int. J. Hydrogen Energy* **2023**, *48*, 6657–6665. [CrossRef]
5. Li, J.S.; Li, L.M.; Wang, J.; Cabot, A.; Zhu, Y.F. Boosting Hydrogen Evolution by Methanol Oxidation Reaction on Ni-Based Electrocatalysts: From Fundamental Electrochemistry to Perspectives. *ACS Energy Lett.* **2024**, *9*, 853–879. [CrossRef]
6. Shen, Q.; Jiang, L.; Zhang, H.; Min, Q.; Hou, W.; Zhu, J.-J. Three-dimensional Dendritic Pt Nanostructures: Sonoelectrochemical Synthesis and Electrochemical Applications. *J. Phys. Chem. C* **2008**, *112*, 16385–16392. [CrossRef]
7. Lu, Q.; Zhao, X.; Luque, R.; Eid, K. Structure-activity relationship of tri-metallic Pt-based nanocatalysts for methanol oxidation reaction. *Coord. Chem. Rev.* **2023**, *493*, 215280. [CrossRef]
8. Liang, J.; Cheng, H.; Zhao, B.; Hu, Q.; Xing, Z.; Zhang, Y.; Niu, L. Boosting the Methanol Oxidation Reaction Activity of Pt-Ru Clusters via Resonance Energy Transfer. *Small* **2023**, *19*, e2302149. [CrossRef]
9. Dong, K.Y.; Dai, H.Z.; Pu, H.K.; Zhang, T.; Wang, Y.Y.; Deng, Y.J. Synthesis of alloyed PtPd nanowires and study on their electro-catalytic performance to methanol oxidation reaction. *Int. J. Hydrogen Energy* **2023**, *48*, 35240–35249. [CrossRef]
10. Wang, Y.F.; Zhang, S.L.; Deng, Y.X.; Luan, S.H.; Wang, C.K.; Ding, L.F.; Jiang, X.; Sun, D.M.; Tang, Y.W. PtPdAg nanotrees with low Pt content for high CO tolerance within formic acid and methanol electrooxidation. *Rare Met.* **2025**, *44*, 300–310. [CrossRef]
11. Li, X.L.; Huang, Y.Q.; Chen, Z.Y.; Hu, S.Q.; Zhu, J.L.; Tsiakaras, P.; Shen, P.K. Novel PtNi nanoflowers regulated by a third element (Rh, Ru, Pd) as efficient multifunctional electrocatalysts for ORR, MOR and HER. *Chem. Eng. J.* **2023**, *454*, 140131. [CrossRef]
12. Kaur, A.; Kaur, G.; Singh, P.P.; Kaushal, S. Supported bimetallic nanoparticles as anode catalysts for direct methanol fuel cells: A review. *Int. J. Hydrogen Energy* **2021**, *46*, 15820–15849. [CrossRef]
13. Pilapil, B.K.; van Drunen, J.; Makonnen, Y.; Beauchemin, D.; Jerkiewicz, G.; Gates, B.D. Ordered Porous Electrodes by Design: Toward Enhancing the Effective Utilization of Platinum in Electrocatalysis. *Adv. Funct. Mater.* **2017**, *27*, 1703171. [CrossRef]
14. Lou, W.H.; Ali, A.; Shen, P.K. Recent development of Au arched Pt nanomaterials as promising electrocatalysts for methanol oxidation reaction. *Nano Res.* **2022**, *15*, 18–37. [CrossRef]
15. Mymoona, P.; Shibu, E.S.; Jeyabharathi, C. Adsorbed Carbon Monoxide-Enabled Self-Terminated Au-Grafting on Pt_6 Nanoclusters for Enhanced Methanol Electrooxidation. *Small* **2024**, *20*, e2401998. [CrossRef]
16. Reddy, G.V.; Sekhar, Y.C.; Raghavendra, P.; Reddy, M.N.; Chandana, P.S.; Sarma, L.S. Controlled synthesis of reduced graphene oxide-supported bimetallic Pt-Au nanoparticles for enhanced electrooxidation of methanol. *Solid State Sci.* **2024**, *149*, 107469. [CrossRef]
17. Wei, K.; Lin, H.; Zhao, X.; Zhao, Z.; Marinkovic, N.; Morales, M.; Huang, Z.; Perlmutter, L.; Guan, H.; Harris, C.; et al. Au/Pt Bimetallic Nanowires with Stepped Pt Sites for Enhanced C–C Cleavage in C2+ Alcohol Electro-oxidation Reactions. *J. Am. Chem. Soc.* **2023**, *145*, 19076–19085. [CrossRef] [PubMed]
18. Kameyama, T.; Sato, K.; Yamamoto, T.; Tamura, M.; Iida, T.; Shoji, T.; Tsuboi, Y.; Torimoto, T. Promoting Oxygen Reduction Reaction by Excitation of Localized Surface Plasmon of Shape- and Facet-Controlled Octahedral Au@Pt Core-Shell Nanocrystals. *Chemelectrochem* **2023**, *10*, e202300182. [CrossRef]
19. Li, C.J.; Liu, S.L.; Yin, S.L.; Yu, H.J.; Wang, Z.Q.; Xu, Y.; Li, X.N.; Wang, L.; Wang, H.J. Facile preparation of Pt-based cage-bell structured nanoarchitectures for enhanced methanol oxidation electrocatalysis. *Int. J. Hydrogen Energy* **2020**, *45*, 2478–2485. [CrossRef]
20. Liang, W.; Wang, Y.; Zhao, L.; Guo, W.; Li, D.; Qin, W.; Wu, H.; Sun, Y.; Jiang, L. 3D Anisotropic Au@Pt–Pd Hemispherical Nanostructures as Efficient Electrocatalysts for Methanol, Ethanol, and Formic Acid Oxidation Reaction. *Adv. Mater.* **2021**, *33*, 2100713. [CrossRef]
21. Fidiani, E.; Thirunavukkarasu, G.; Li, Y.; Chiu, Y.L.; Du, S.F. Au integrated AgPt nanorods for the oxygen reduction reaction in proton exchange membrane fuel cells. *J. Mater. Chem. A* **2021**, *9*, 5578–5587. [CrossRef]
22. Lee, S.; Lee, J.; Lee, S.; Haddadnezhad, M.; Oh, M.J.; Zhao, Q.; Yoo, S.; Liu, L.; Jung, I.; Park, S. Multi-Layered PtAu Nanoframes and Their Light-Enhanced Electrocatalytic Activity via Plasmonic Hot Spots. *Small* **2023**, *19*, e2206377. [CrossRef] [PubMed]
23. Rey-Raap, N.; dos Santos-Gomez, L.; Arenillas, A. Carbons for fuel cell energy generation. *Carbon* **2024**, *228*, 119291. [CrossRef]
24. Huang, X.J.; Yarimaga, O.; Kim, J.H.; Choi, Y.K. Substrate surface roughness-dependent 3-D complex nanoarchitectures of gold particles from directed electrodeposition. *J. Mater. Chem.* **2009**, *19*, 478–483. [CrossRef]

25. Yu, M.; Chen, J.; Liu, J.; Li, S.; Ma, Y.; Zhang, J.; An, J. Mesoporous $NiCo_2O_4$ nanoneedles grown on 3D graphene-nickel foam for supercapacitor and methanol electro-oxidation. *Electrochim. Acta* **2015**, *151*, 99–108. [CrossRef]
26. Samad, S.; Loh, K.S.; Wong, W.Y.; Lee, T.K.; Sunarso, J.; Chong, S.T.; Daud, W.R.W. Carbon and non-carbon support materials for platinum-based catalysts in fuel cells. *Int. J. Hydrogen Energy* **2018**, *43*, 7823–7854. [CrossRef]
27. Parvez, K.; Wu, Z.-S.; Li, R.; Liu, X.; Graf, R.; Feng, X.; Muellen, K. Exfoliation of Graphite into Graphene in Aqueous Solutions of Inorganic Salts. *J. Am. Chem. Soc.* **2014**, *136*, 6083–6091. [CrossRef]
28. Xiang, X.; Feng, S.; Chen, J.; Feng, J.; Hou, Y.; Ruan, Y.; Weng, X.; Milcovich, G. Gold Nanoparticles/Electrochemically Expanded Graphite Composite: A Bifunctional Platform toward Glucose Sensing and SERS Applications. *J. Electroanal. Chem.* **2019**, *851*, 113471. [CrossRef]
29. Yu, L.; Lv, M.-Y.; Zhang, T.; Zhou, Q.; Zhang, J.; Weng, X.; Ruan, Y.; Feng, J. In Situ Growth of Self-Supported CuO Nanorods from Cu-MOFs for Glucose Sensing and Elucidation of the Sensing Mechanism. *Anal. Methods* **2024**, *16*, 731–741. [CrossRef]
30. Trasatti, S.; Petrii, O.A. Real surface area measurements in electrochemistry. *J. Electroanal. Chem.* **1992**, *327*, 353–376. [CrossRef]
31. Habibi, B.; Ghaderi, S. Synthesis, characterization and electrocatalytic activity of Co@Pt nanoparticles supported on carbon-ceramic substrate for fuel cell applications. *Int. J. Hydrogen Energy* **2015**, *40*, 5115–5125. [CrossRef]
32. Nagar, B.; Balsells, M.; de la Escosura-Muñiz, A.; Gomez-Romero, P.; Merkoçi, A. Fully Printed One-Step Biosensing Device Using Graphene/AuNPs Composite. *Biosens. Bioelectron.* **2019**, *129*, 238–244. [CrossRef]
33. Li, J.; Jilani, S.Z.; Lin, H.; Liu, X.; Wei, K.; Jia, Y.; Zhang, P.; Chi, M.; Tong, Y.J.; Xi, Z.; et al. Ternary CoPtAu Nanoparticles as a General Catalyst for Highly Efficient Electro-oxidation of Liquid Fuels. *Angew. Chem.-Int. Ed.* **2019**, *58*, 11527–11533. [CrossRef] [PubMed]
34. Zhang, Z.; Wang, Y.; Wang, X. Nanoporous bimetallic Pt-Au alloy nanocomposites with superior catalytic activity towards electro-oxidation of methanol and formic acid. *Nanoscale* **2011**, *3*, 1663–1674. [CrossRef]
35. Gowthaman, N.S.K.; Sinduja, B.; Shankar, S.; John, S.A. Displacement reduction routed Au-Pt bimetallic nanoparticles: A highly durable electrocatalyst for methanol oxidation and oxygen reduction. *Sustain. Energy Fuels* **2018**, *2*, 1588–1599. [CrossRef]
36. Chen, C.-S.; Pan, F.-M.; Yu, H.-J. Electrocatalytic activity of Pt nanoparticles on a karst-like Ni thin film toward methanol oxidation in alkaline solutions. *Appl. Catal. B-Environ.* **2011**, *104*, 382–389. [CrossRef]
37. Ren, F.; Zhai, C.; Zhu, M.; Wang, C.; Wang, H.; Bin, D.; Guo, J.; Yang, P.; Du, Y. Facile synthesis of PtAu nanoparticles supported on polydopamine reduced and modified graphene oxide as a highly active catalyst for methanol oxidation. *Electrochim. Acta* **2015**, *153*, 175–183. [CrossRef]
38. Ji, Z.; Zhu, G.; Shen, X.; Zhou, H.; Wu, C.; Wang, M. Reduced graphene oxide supported FePt alloy nanoparticles with high electrocatalytic performance for methanol oxidation. *New J. Chem.* **2012**, *36*, 1774–1780. [CrossRef]
39. Jeong, H.; Kim, J. Methanol dehydrogenation reaction at Au@Pt catalysts: Insight into the methanol electrooxidation. *Electrochim. Acta* **2018**, *283*, 11–17. [CrossRef]
40. Jia, H.; Chang, G.; Shu, H.; Xu, M.; Wang, X.; Zhang, Z.; Liu, X.; He, H.; Wang, K.; Zhu, R.; et al. Pt nanoparticles modified Au dendritic nanostructures: Facile synthesis and enhanced electrocatalytic performance for methanol oxidation. *Int. J. Hydrogen Energy* **2017**, *42*, 22100–22107. [CrossRef]
41. Kang, J.; Nam, S.; Oh, Y.; Choi, H.; Wi, S.; Lee, B.; Hwang, T.; Hong, S.; Park, B. Electronic Effect in Methanol Dehydrogenation on Pt Surfaces: Potential Control during Methanol Electrooxidation. *J. Phys. Chem. Lett.* **2013**, *4*, 2931–2936. [CrossRef]
42. Fang, J.; Zhang, Y.; Zhou, Y.; Zhao, S.; Zhang, C.; Zhang, H.; Sheng, X. In-situ formation of supported Au nanoparticles in hierarchical yolk-shell CeO_2 /$mSiO_2$ structures as highly reactive and sinter-resistant catalysts. *J. Colloid Interface Sci.* **2017**, *488*, 196–206. [CrossRef] [PubMed]
43. Cui, X.; Wang, J.; Liu, B.; Ling, S.; Long, R.; Xiong, Y. Turning Au Nanoclusters Catalytically Active for Visible-Light-Driven CO_2 Reduction through Bridging Ligands. *J. Am. Chem. Soc.* **2018**, *140*, 16514–16520. [CrossRef]
44. van Spronsen, M.A.; Frenken, J.W.M.; Groot, I.M.N. Observing the oxidation of platinum. *Nat. Commun.* **2017**, *8*, 429. [CrossRef]
45. Huang, D.; Qi, Y.; Bai, X.; Shi, L.; Jia, H.; Zhang, D.; Zheng, L. One-Pot Synthesis of Dendritic Gold Nanostructures in Aqueous Solutions of Quaternary Ammonium Cationic Surfactants: Effects of the Head Group and Hydrocarbon Chain Length. *ACS Appl. Mater. Interfaces* **2012**, *4*, 4665–4671. [CrossRef] [PubMed]
46. Imai, H. Self-Organized Formation of Hierarchical Structures. In *Biomineralization I*; Springer: Berlin/Heidelberg, Germany, 2007; pp. 43–72. [CrossRef]
47. Ye, W.; Yan, J.; Ye, Q.; Zhou, F. Template-Free and Direct Electrochemical Deposition of Hierarchical Dendritic Gold Microstructures: Growth and Their Multiple Applications. *J. Phys. Chem.* **2010**, *114*, 15617–15624. [CrossRef]
48. Xia, Y.; Xiong, Y.; Lim, B.; Skrabalak, S.E. Shape-Controlled Synthesis of Metal Nanocrystals: Simple Chemistry Meets Complex Physics? *Angew. Chem.-Int. Ed.* **2009**, *48*, 60–103. [CrossRef]
49. Feng, L.; Wu, X.; Ren, L.; Xiang, Y.; He, W.; Zhang, K.; Zhou, W.; Xie, S. Crystal Growth & Design of Au@Pt Nanostructures by Gold-Nanorod-Seeded Growth. *Chem.-A Eur. J.* **2008**, *14*, 9764–9771. [CrossRef]

50. Fu, T.; Fang, J.; Wang, C.; Zhao, J. Hollow porous nanoparticles with Pt skin on a Ag-Pt alloy structure as a highly active electrocatalyst for the oxygen reduction reaction. *J. Mater. Chem. A* **2016**, *4*, 8803–8811. [CrossRef]
51. Wang, L.; Hu, C.; Nemoto, Y.; Tateyama, Y.; Yamauchi, Y. On the Role of Ascorbic Acid in the Synthesis of Single-Crystal Hyperbranched Platinum Nanostructures. *Cryst. Growth Des.* **2010**, *10*, 3454–3460. [CrossRef]
52. Ponomarev, I.I.; Skupov, K.M.; Zhigalina, O.M.; Khmelenin, D.N.; Ponomarev, I.I.; Vtyurina, E.S.; Cherkovskiy, E.N.; Basu, V.G.; Modestov, A.D. Deposition of Pt Nanoparticles by Ascorbic Acid on Composite Electrospun Polyacrylonitrile-Based Carbon Nanofiber for HT-PEM Fuel Cell Cathodes. *Catalysts* **2022**, *12*, 891. [CrossRef]
53. Chen, S.; Wu, H.; Tao, J.; Xin, H.; Zhu, Y.; Chen, J. Pt-Ni Seed-Core-Frame Hierarchical Nanostructures and Their Conversion to Nanoframes for Enhanced Methanol Electro-Oxidation. *Catalysts* **2019**, *9*, 39. [CrossRef]